

Article

Effect of Magnetic Field and Hydrostatic Pressure on Metamagnetic Isostructural Phase Transition and Multicaloric Response of Fe₄₉Rh₅₁ Alloy

Alexander P. Kamantsev ¹, Abdulkarim A. Amirov ^{2,*}, Vladislav D. Zaporozhets ³, Igor F. Griбанov ³, Aleksay V. Golovchan ³, Victor I. Valkov ³, Oksana O. Pavlukhina ⁴, Vladimir V. Sokolovskiy ^{4,5}, Vasiliy D. Buchelnikov ⁴, Akhmed M. Aliev ² and Victor V. Koledov ¹

¹ Kotelnikov Institute of Radioengineering and Electronics of Russian Academy of Sciences, 125009 Moscow, Russia; kaman4@gmail.com (A.P.K.)

² Amirkhanov Institute of Physics, Dagestan Scientific Center of Russian Academy of Sciences, 367003 Makhachkala, Russia; lowtemp@mail.ru

³ Galkin Donetsk Institute for Physics and Engineering, 283050 Donetsk, Russia

⁴ Department of Condensed Matter Physics, Chelyabinsk State University, 454001 Chelyabinsk, Russia; buche@csu.ru (V.D.B.)

⁵ Academic Research Center for Energy Efficiency, National University of Science and Technology "MISIS", 119049 Moscow, Russia

* Correspondence: amiroff_a@mail.ru

Abstract: The effect of a high magnetic field up to 12 T and a high hydrostatic pressure up to 12 kbar on the stability of the metamagnetic isostructural phase transition and the multicaloric effect of Fe₄₉Rh₅₁ alloy has been studied. The phase transition temperature shifts under the magnetic field and the hydrostatic pressure on with the rates of $dT_m/\mu_0dH = -9.2$ K/T and $dT_m/dP = 3.4$ K/kbar, respectively. The magnetocaloric and multicaloric (under two external fields) effects were studied via indirect method using Maxwell relations. The maximum of the entropy change is increasing toward the high temperature region from $\Delta S \sim 2.5$ J/(kg K) at 305 K to $\Delta S \sim 2.7$ J/(kg K) at 344 K under simultaneously applied magnetic field of 0.97 T and hydrostatic pressure of 12 kbar. The obtained results were explained using the first-principle calculations of Gibbs energies and the phonon spectra of the ferromagnetic and the antiferromagnetic phases. Taking into account the low concentration of antisite defects in the calculation cells allows us to reproduce the experimental dT_m/dP coefficient.

Keywords: FeRh alloys; metamagnetic phase transition; magnetocaloric effect; multicaloric effect; high pressure; high magnetic fields; ab initio calculations



Citation: Kamantsev, A.P.; Amirov, A.A.; Zaporozhets, V.D.; Griбанov, I.F.; Golovchan, A.V.; Valkov, V.I.; Pavlukhina, O.O.; Sokolovskiy, V.V.; Buchelnikov, V.D.; Aliev, A.M.; et al. Effect of Magnetic Field and Hydrostatic Pressure on Metamagnetic Isostructural Phase Transition and Multicaloric Response of Fe₄₉Rh₅₁ Alloy. *Metals* **2023**, *13*, 956. <https://doi.org/10.3390/met13050956>

Academic Editor: Eric Hug

Received: 17 April 2023

Revised: 5 May 2023

Accepted: 8 May 2023

Published: 15 May 2023



Copyright: © 2023 by the authors. Licensee MDPI, Basel, Switzerland. This article is an open access article distributed under the terms and conditions of the Creative Commons Attribution (CC BY) license (<https://creativecommons.org/licenses/by/4.0/>).

1. Introduction

The FeRh alloys with the near-equiatomic composition are characterized by a CsCl-type crystal structure with a first-order magnetic phase transition from the antiferromagnetic (AFM) state to the ferromagnetic (FM) at the same average temperature T_m , which depends strongly on the chemical composition [1–3]. These alloys exhibit significant changes in the magnetization and lattice parameter without the change in the crystal symmetry in the vicinity of the T_m [4], which can be called the magnetovolume effect at the metamagnetic isostructural phase transition (MIPT). The FeRh alloys are convenient model objects for studying the nature of the MIPT, due to their simple crystal structure and the bright effects observed near T_m . There are several methods to control the MIPT temperature in FeRh alloys such as a magnetic field [5], a hydrostatic pressure [6], an electric field-induced strain [7–9], a heat treatment [10,11], a chemical substitution [12], and an ion irradiation [13]. The first studies of the temperature dependences of magnetization, Young's modulus, and the crystal lattice parameter were carried out via dilatometric method on the equiatomic alloy Fe₅₀Rh₅₀ [2], and the rates of MIPT temperature shift

dT_m/dP and $dT_m/\mu_0 dH$ in the hydrostatic pressure p and the magnetic field $\mu_0 H$ were estimated. The FeRh alloys exhibit high magnetization saturation up to $130 \text{ Am}^2/\text{kg}$ in the FM phase [14], and the MIPT is accompanied by a strong anomaly of the specific heat capacity [15] and an isotropic volume increase of $\sim 1\%$ [2]. The magnetostriction of the $\text{Fe}_{50}\text{Rh}_{50}$ alloy was firstly measured in the temperature range 290–400 K in magnetic fields up to 15 T [16]. The published phase diagrams for near-equiatomic FeRh alloys as a function of a magnetic field and a pressure present the collected data of the theoretical calculations and the experimental results obtained from the samples with different compositions and fabrication protocols [17–19]. For example, the P – T and the $\mu_0 H$ – T diagrams obtained from experimental data for $\text{Fe}_{49}\text{Rh}_{51}$ alloy are limited by the hydrostatic pressure of 5 kbar [19] and the magnetic fields of 6 T [20].

The FeRh alloys have a number of unique functional properties in the external magnetic and mechanical fields known as “giant” caloric and multicaloric effects [17,19–23] due to the phenomena near T_m described above. The large magnetocaloric effect (MCE) [21], the elastocaloric effect [22] and the barocaloric effect (BCE) [20] were observed in FeRh alloys near the MIPT temperatures. For the first time, the MCE in the $\text{Fe}_{48}\text{Rh}_{52}$ alloy was reported in [24], where the dependence of the critical magnetic field on the MIPT temperature was established and the observed inverse MCE (the decreasing of the sample temperature under increasing of the external magnetic field) was described as a negative factor for constructing the critical magnetic field diagram. The near-equiatomic FeRh alloys were proposed as promising materials for the magnetic cooling at the room temperatures due to record values of MCE, where the values of the adiabatic temperature changes were as follows: $\Delta T_{ad} = -12.9 \text{ K}$ at $\mu_0 \Delta H = 1.95 \text{ T}$ in the $\text{Fe}_{49}\text{Rh}_{51}$ [21,25]; $\Delta T_{ad} = -20.2 \text{ K}$ at $\mu_0 \Delta H = 8 \text{ T}$ in the $\text{Fe}_{48}\text{Rh}_{52}$ [26]. In addition, the MCE was studied via the direct method in pulsed fields $\mu_0 \Delta H = 50 \text{ T}$ in the $\text{Fe}_{49}\text{Rh}_{51}$ alloy [27]. The BCE in $\text{Fe}_{49}\text{Rh}_{51}$ alloys was studied under hydrostatic pressure up to 2.5 kbar [20,28]. The effect of the magnetic field and the hydrostatic pressure on the MIPT through the electrical resistance measurements were demonstrated in $(\text{Fe}_{1-x}\text{Ni}_x)_{49}\text{Rh}_{51}$ alloys at the hydrostatic pressure up to 13 kbar [29], as well as in the $\text{Fe}_{48}\text{Rh}_{52}$ alloy at the applied magnetic field up to 8 T [30].

One of the promising approaches of the solid-state cooling based on the caloric effects is the multicaloric approach, which is based on the combination of the different external fields (magnetic, mechanical, electric) [31,32]. The multicaloric approach based on the combination of the MCE and the BCE under the external magnetic field up to 5 T and the hydrostatic pressure up to 5 kbar was experimentally used for the $\text{Fe}_{49}\text{Rh}_{51}$ alloy [19]. Moreover, the uniaxial mechanical force can be used to improve the efficiency of systems operating on MCEs in magnetic materials with the first-order phase transitions [23,33]. The uniaxial compression in combination with the magnetic field can be used to control hysteresis effects that negatively contribute to the efficiency of magnetic cooling systems [34].

The present work is aimed to investigate the two interrelated phenomena in FeRh alloys within the framework of a single study: (1) the effect of the combination of the magnetic field and the hydrostatic pressure on the temperature of the phase transition; and (2) the measurements of the multicaloric effect in magnetic field combined with the hydrostatic pressure. The FeRh samples with the same $\text{Fe}_{49}\text{Rh}_{51}$ composition but with two different heat treatment protocols were used as an object. The ab initio approach, which includes the total energy and the phonons calculations, was employed in order to describe the experimental P – T diagram.

2. Materials and Methods

The ingot of $\text{Fe}_{49}\text{Rh}_{51}$ alloy was obtained via induction melting in an argon atmosphere. The samples in shape of the disks with a diameter of 5 mm and thickness of 1 mm were cut out of the ingot. The samples were annealed in the pre-pumped quartz ampoules ($\sim 1 \text{ Pa}$) at a temperature of 1273 K. The first series of $\text{Fe}_{49}\text{Rh}_{51}$ samples was annealed for 72 h and quenched in ice water following this—the *FR72h* samples—and the second series was annealed for 48 h and cooled in the furnace—the *FR48h* samples. The structure and the

elemental composition of the samples were confirmed via energy dispersion spectroscopy (EDS) and X-ray diffraction analysis (XRD) and presented in earlier work [35]. The MIPT temperatures of *FR72h* and *FR48h* samples were determined using two different methods: (1) the differential scanning calorimetry (DSC) on the calorimeter Netzsch DSC 204F1 Phoenix in zero magnetic field; and (2) the temperature magnetometry on the vibration magnetometer Versa Lab Quantum Design in a low magnetic field of 1 mT. The rate of the temperature change in these experiments was 10 K/min.

The magnetic field dependences of the magnetization of *FR72h* sample at the different temperatures in vicinity of the MIPT (300–328 K) were measured using the vibration magnetometer Quantum Design PPMS-14T in the magnetic field up to 8 T. The temperature dependences of the electrical resistance of *FR72h* sample at the different magnetic fields (0–12 T) were measured using the four-point method on Quantum Design PPMS-14T with the insert for the transport properties measurements. The experiments for studies of the multicaloric effects near the MIPT of *FR48h* sample at simultaneously applied magnetic field (0.155 T or 0.97 T) and hydrostatic pressure (up to 12 kbar) were carried out using the Domenicali-type pendulum magnetometer [36]. The mass of the *FR48h* sample was approximately 12.5 mg. The non-magnetic high-pressure cells with the sample were mounted at the end of the pendulum. This cell was made of the beryllium bronze, and pure indium (In) was used as the pressure transmitting medium. The pressure in the cell was determined based on the calibration of this system on chromium telluride (CrTe), which has the well-known phase transition temperatures shift on the applied pressure of -6 K/kbar. The MCE and the multicaloric effect were estimated via indirect method with the help of the well-known Maxwell relations.

The theoretical study of the ground-state properties of FeRh alloy was conducted using the density functional theory (DFT) calculations within the projector augmented wave method (PAW) method as implemented in the VASP package [37,38]. To describe the exchange correlation effects, both the generalized-gradient approximation (GGA) in the form of Perdew–Burke–Ernzerhof (PBE) [39] and the recently developed strongly constrained and appropriately normed (SCAN) meta-GGA [40] were used for the exchange correlation functional. The PAW potentials were selected with the following set of valence electrons: $3p^63d^74s^1$ for Fe and $4p^64d^85s^1$ for Rh. The plane wave cut-off parameter was taken as 700 eV and the Brillouin zone sampling is confined to $8 \times 8 \times 8$ k -mesh generated by the Monkhorst-Pack scheme. The 16-atom cubic supercell with the space group $Fm-3m$ and FM, AFM orders of Fe atoms was taken into account in the geometry optimization calculations. The zero temperature phonon spectrum calculations was performed in the harmonic approximation considering the small displacement method (0.01 Å) as implemented in the Phonopy package [41]. The $2 \times 2 \times 2$ (32 atoms) supercell with four basis atoms in a *fcc* unit cell for AFM phase and $3 \times 3 \times 3$ (54 atoms) supercell with two basis atoms in a *bcc* unit cell for FM phase were chosen. In order to investigate the thermodynamic properties of the FeRh under temperature and pressure, the quasi-harmonic Debye model implemented in the GIBBS code [42,43] was applied.

3. Results and Discussion

3.1. Experimental Studies

The DSC thermograms at the heating and cooling protocols for *FR72h* and *FR48h* samples are shown in Figure 1 (left axes). The temperatures of the start (AF_S and F_S) and the finish (AF_F and F_F) of the MIPT for the *FR72h* sample were determined from the DSC curves (Figure 1a) as $AF_S = 317$ K, $AF_F = 308$ K at cooling (from FM to AFM state) and $F_S = 321$ K, $F_F = 330$ K at heating (from AFM to FM state). The latent heat of the MIPT for *FR72h* sample was calculated as the area under the DSC peaks: $\lambda_C = 4300$ J/kg at cooling, and $\lambda_H = 4400$ J/kg at heating (Figure 1a). The corresponding MIPT temperatures for the *FR48h* sample were determined to be $AF_S = 316$ K, $AF_F = 295$ K at cooling and $F_S = 306$ K, $F_F = 328$ K at heating (Figure 1b). The latent heat of the MIPT for *FR48h* sample was as follows: $\lambda_C = 4300$ J/kg at cooling, and $\lambda_H = 3600$ J/kg at heating (Figure 1b).

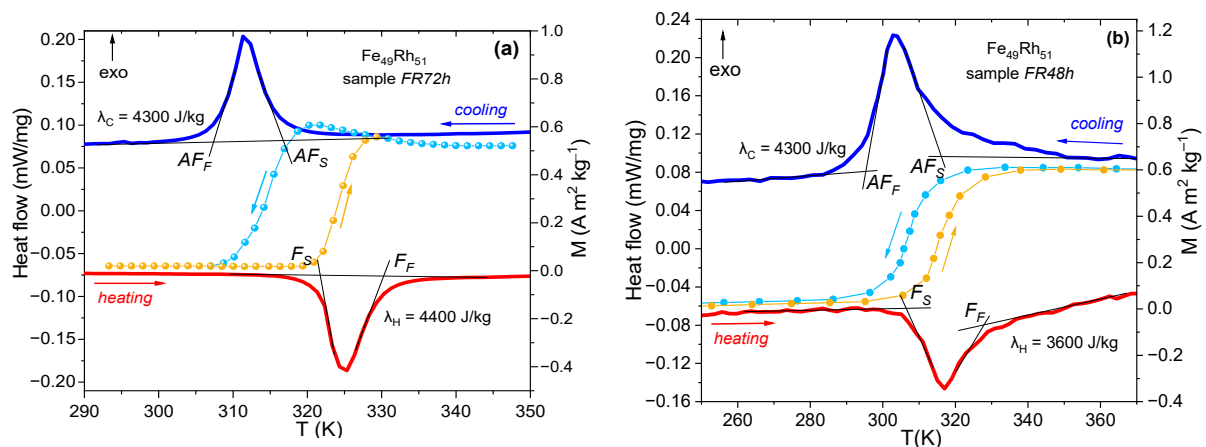


Figure 1. DSC thermograms in zero magnetic field (left axis) and temperature dependences of the magnetization in low magnetic field of 1 mT (right axis) for (a) *FR72h* and (b) *FR48h* samples of $\text{Fe}_{49}\text{Rh}_{51}$ alloy.

The temperature dependences of the magnetization for *FR72h* and *FR48h* samples at heating and cooling in low magnetic field of 1 mT are shown in Figure 1 (right axes). These curves show the temperature hysteresis of the first order MIPT between two phases of $\text{Fe}_{49}\text{Rh}_{51}$: AFM at lower temperatures and FM at higher temperatures. The MIPT temperatures obtained from the DSC analysis are consistent with the temperatures from magnetometry data with an accuracy of 1 K (Figure 1a,b). In general, the differences in the heat treatment of the *FR72h* and *FR48h* samples greatly affected on AF_F and F_S temperatures (lower in *FR48h*).

Figure 2a demonstrates the magnetic field dependences of the magnetization $M(\mu_0 H)$ for *FR72h* sample at different temperatures from the range 300–328 K in magnetic field of 8 T. The magnetic field-induced MIPT is observed in Figure 2a, similar to that were observed in $\text{Fe}_{48}\text{Rh}_{52}$ alloy in [44]. The magnetization hysteresis at the lowest temperature (300 K, the black curve in Figure 2a) is wide because the sample initially is completely in the AFM phase (lower than $AF_F = 308$ K). The magnetization hysteresis at highest temperature (328 K, the yellow curve in Figure 2a) is narrow because, initially, the sample is close to complete transition to the FM phase ($F_F = 330$ K).

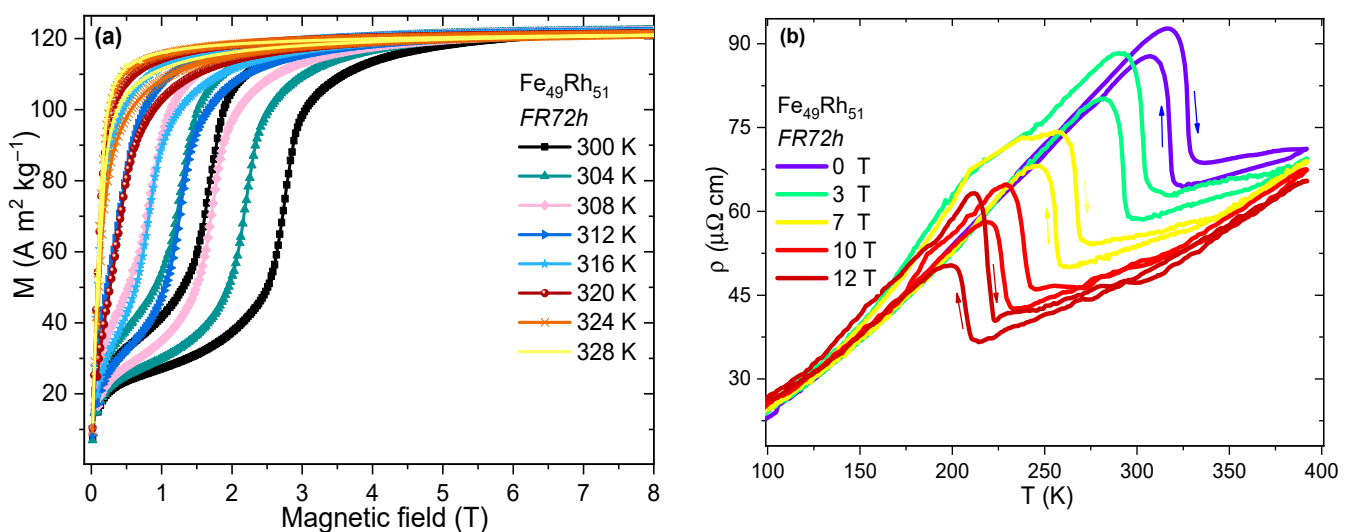


Figure 2. (a) Magnetization isotherms for *FR72h* sample of $\text{Fe}_{49}\text{Rh}_{51}$ alloy at different temperatures in the 300–328 K range in magnetic field of 8 T. (b) Temperature dependences of the electrical resistivity for *FR72h* sample of $\text{Fe}_{49}\text{Rh}_{51}$ alloy at heating and cooling at different magnetic fields in the 0–12 T range.

Figure 2b demonstrates the temperature dependences of the electrical resistivity for the *FR72h* sample at heating and cooling at different magnetic fields up to 12 T. These measurements show the shifts in the MIPT temperatures under the high magnetic fields. The temperature hysteresis of the MIPT in $\text{Fe}_{49}\text{Rh}_{51}$ alloy according to the measurements results shifts to the lower temperature region with the increasing in magnetic fields, which is explained by the presence of the nuclei of the high-temperature FM phase at the low temperatures. Additionally, as a result, some broadening of the temperature hysteresis is observed with the increasing of the external magnetic field (Figure 3b), which is in good agreement with the results obtained for the $\text{Fe}_{48}\text{Rh}_{52}$ alloy [30].

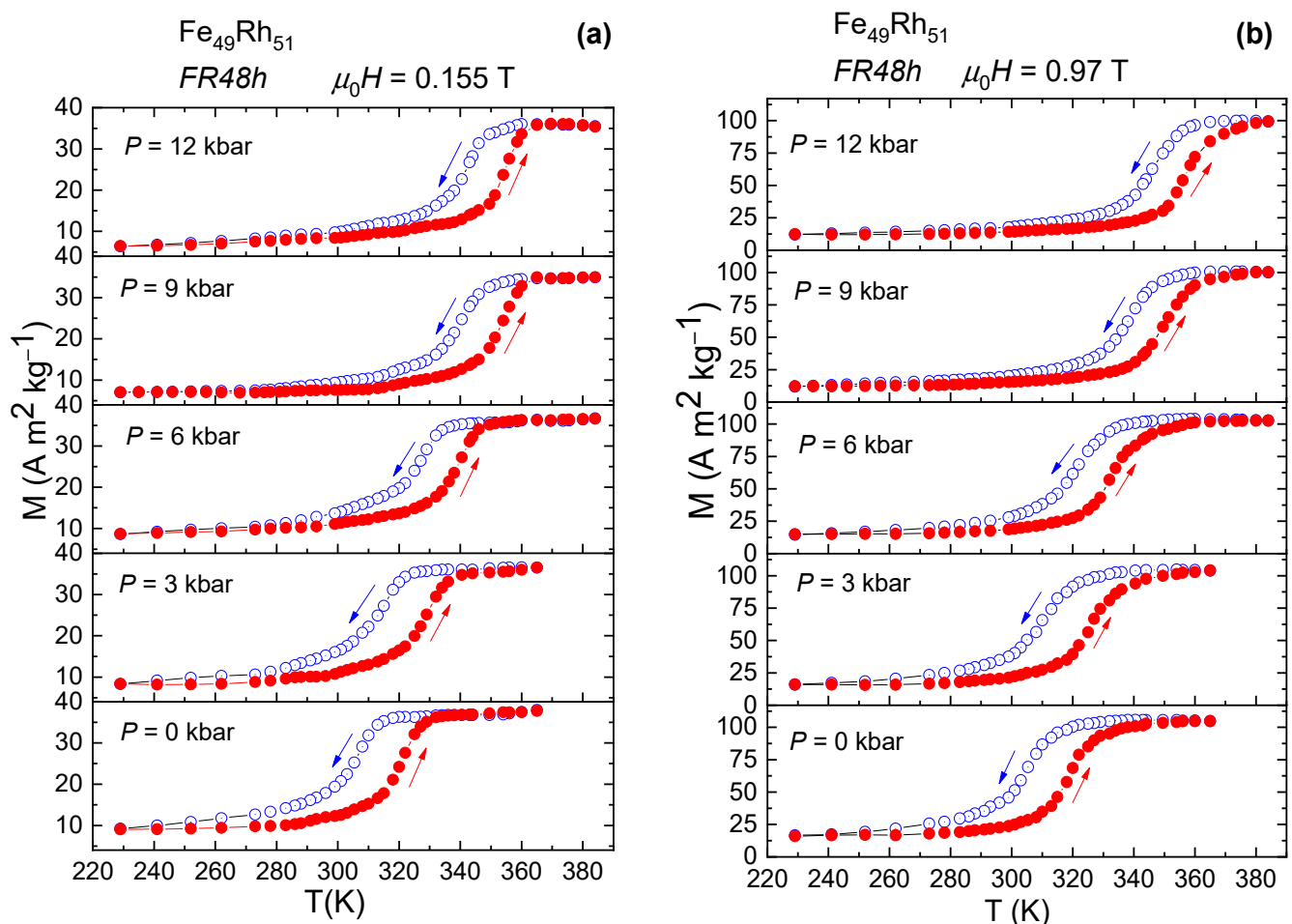


Figure 3. Temperature dependences of the magnetization for *FR48h* sample of $\text{Fe}_{49}\text{Rh}_{51}$ alloy measured under combined hydrostatic pressure in the 0–12 kbar range and magnetic field of (a) 0.155 T and (b) 0.97 T.

Figure 3 demonstrates the temperature dependences of the magnetization of the *FR48h* sample at applied hydrostatic pressure from 0 to 12 kbar in magnetic fields of 0.155 T (Figure 3a) and 0.97 T (Figure 3b). The temperature hysteresis of the MIPT in the $\text{Fe}_{49}\text{Rh}_{51}$ alloy shifts to the higher temperatures region with the increase in hydrostatic pressure, and there is a certain narrowing of the temperature hysteresis at the same time. This is explained by the strong magneto-elastic coupling between the magnetic and structural subsystems in the solid. The external hydrostatic pressure compresses the crystal lattice and thus blocks the origination of the high-temperature FM phase with the larger unit cell volume. However, studies in such a range of magnetic fields and pressures for FeRh alloys are not known in the literature, and this would certainly expand our knowledge about the nature of the MIPT of these alloys.

If both the magnetization and the entropy are continuous functions of the temperature and the magnetic field, then an infinitesimal change in isobaric-isothermal entropy can be associated with the magnetization M , the magnetic field strength H and the absolute temperature T using one of Maxwell's relations in integral form [45–47]:

$$\Delta S_{mag} = \mu_0 \int_0^H \left(\frac{\partial M}{\partial T} \right) dH \quad (1)$$

It is possible to calculate the magnetic entropy change ΔS in *FR72h* sample of $\text{Fe}_{49}\text{Rh}_{51}$ alloy connected with the external magnetic field change via Equation (1) using the data of the isothermal magnetization in Figure 2a. The calculation results for $\mu_0\Delta H = 1$ and 2 T are shown in Figure 4a, while the maximum value was $\Delta S = 5.6 \text{ J}/(\text{kg K})$ at $\mu_0\Delta H = 1 \text{ T}$. This result correlates well with the calculated data from the heat capacity measurement in [48]: $\Delta S = 5.5 \text{ J}/(\text{kg K})$ at $\mu_0\Delta H = 1 \text{ T}$ for $\text{Fe}_{49}\text{Rh}_{51}$ alloy.

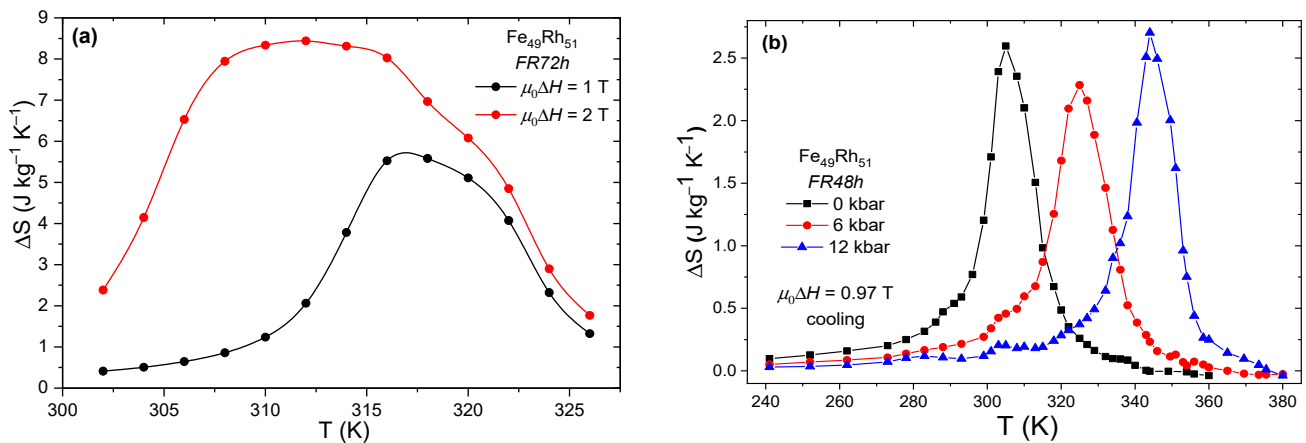


Figure 4. (a) Temperature dependences of the magnetic entropy change ΔS for *FR72h* sample at magnetic field changes $\mu_0\Delta H = 1 \text{ T}$ and 2 T, calculated from Figure 2a using Equation (1). (b) Temperature dependences of ΔS for *FR48h* sample at $\mu_0\Delta H = 0.97 \text{ T}$ under applied hydrostatic pressure 0 kbar, 6 kbar, 12 kbar at cooling protocol, calculated from Figure 3b using Equation (1).

Additionally, it is possible to calculate the magnetic entropy change ΔS in *FR48h* sample of $\text{Fe}_{49}\text{Rh}_{51}$ alloy connected with the external magnetic field change via Equation (1) using the data of the magnetization under different external pressures in Figure 3b. The calculation results for $\mu_0\Delta H = 0.97 \text{ T}$ at cooling protocol are shown in Figure 4b, while the maximum obtained value was $\Delta S = 2.7 \text{ J}/(\text{kg K})$ under the external pressure $p = 12 \text{ kbar}$. Thus, there is the difference in ΔS more than 2 times for *FR72h* and *FR48h* samples at the magnetic field changes of 1 T, which is explained by the difference in the heat treatment of the samples.

The magnetic phase μ_0H - T diagram based on the data of the temperature dependence of the electrical resistance for *FR72h* sample of $\text{Fe}_{49}\text{Rh}_{51}$ alloy in high magnetic fields was presented in Figure 5. The MIPT temperatures in different magnetic fields up to 12 T from Figure 2b were plotted on phase μ_0H - T diagram. It was established that the magnetic field shifts the MIPT to the region of the lower temperatures with the average rate $dT_m/\mu_0dH = -9.2 \text{ K}/\text{T}$. The obtained value generally corresponds with known data in the literature for the $\text{Fe}_{49}\text{Rh}_{51}$ alloy [20]: $dT_m/\mu_0dH = -9.6 \text{ K}/\text{T}$ in magnetic field up to 6 T.

The phase P - T diagram based on the data of the temperature dependence of the magnetization (at 0.97 T) for *FR48h* sample of $\text{Fe}_{49}\text{Rh}_{51}$ alloy under the high hydrostatic pressure is presented in Figure 5. The MIPT temperatures in different external hydrostatic pressures up to 12 kbar from Figure 3b were plotted in the P - T diagram. The restores stability of the AFM order and shifts the MIPT to the region of higher temperatures with

the average rate $dT_m/dP = 3.4$ K/kbar. The obtained value is lower than the data presented in the literature for the $\text{Fe}_{49}\text{Rh}_{51}$ alloy [20]: $dT_m/dP = 6.4$ K/kbar in hydrostatic pressure up to 2.5 kbar—this discrepancy is explained by the difference in the heat treatment of the samples.

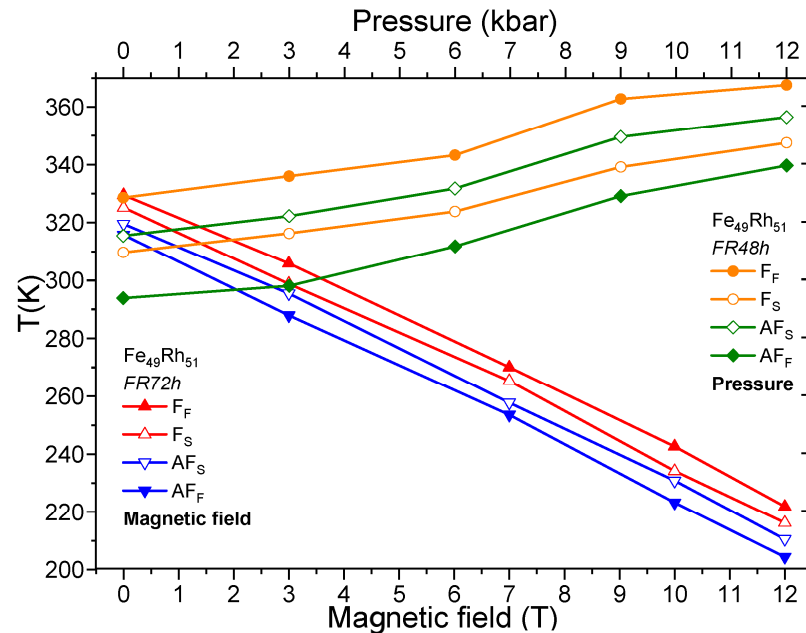


Figure 5. μ_0H - T phase diagram for *FR72h* sample is obtained from Figure 2b and P - T phase diagram for *FR48h* sample is obtained from Figure 3b.

3.2. DFT Calculations

Since Fe-based alloys belong to strongly correlated electronic systems, there is an interest in studying the exchange correlation effects on the ground state properties of the AFM and FM phases of FeRh compound. Figure 6a displays the total energy difference as a function of lattice constant with respect to the AFM ground state calculated with PBE and SCAN. To find an optimized lattice parameter, the energy curves are fitted to the Birch-Murnaghan equation of state. As can be seen that both functionals predict the AFM order as energetically favorable. However, for both types of magnetic ordering, the SCAN lattice parameters (2.981 Å and 2.962 Å for FM and AFM) are found to be slightly smaller than those of the PBE one (3.003 Å and 2.988 Å for FM and AFM). It is worth noting that additional electron correlation effects beyond the GGA yield a significantly smaller energy difference ΔE (by approximately an order of magnitude) in comparison to that of PBE. Thus, the calculated SCAN value is $\Delta E = 2.3$ meV/atom. In regard to the magnetic moments, the SCAN slightly overestimates them compared to those for the PBE. This is a known feature of the SCAN functional due to self-interaction corrections, which can be measured using the Coulomb energy U [49–53].

Next, let us discuss the phonon spectra for the AFM phase, which are calculated in the harmonic approximation using the SCAN and PBE functionals. It should be noted that we omit the results for the FM case here, since they show similar behavior without any sign of instability, as reported in earlier DFT calculations (e.g., Refs. [54–56]). As evident from Figure 6b, the PBE calculations demonstrate the phonon instability observed at the X point that contradicts the experimental data. On the other side, the meta-GGA calculations lead to the degeneracy of the anomaly of the optical phonon spectrum at the X point, thereby making the AFM phase dynamically stable at 0 K as in a case of FM phase. In general, a similar phonon spectra can be observed for both FM and AFM phases. The calculated Debye temperatures Θ_D from the phonon dispersion relations are found to be approximately 370 K and 394 K for FM and AFM phase, respectively.

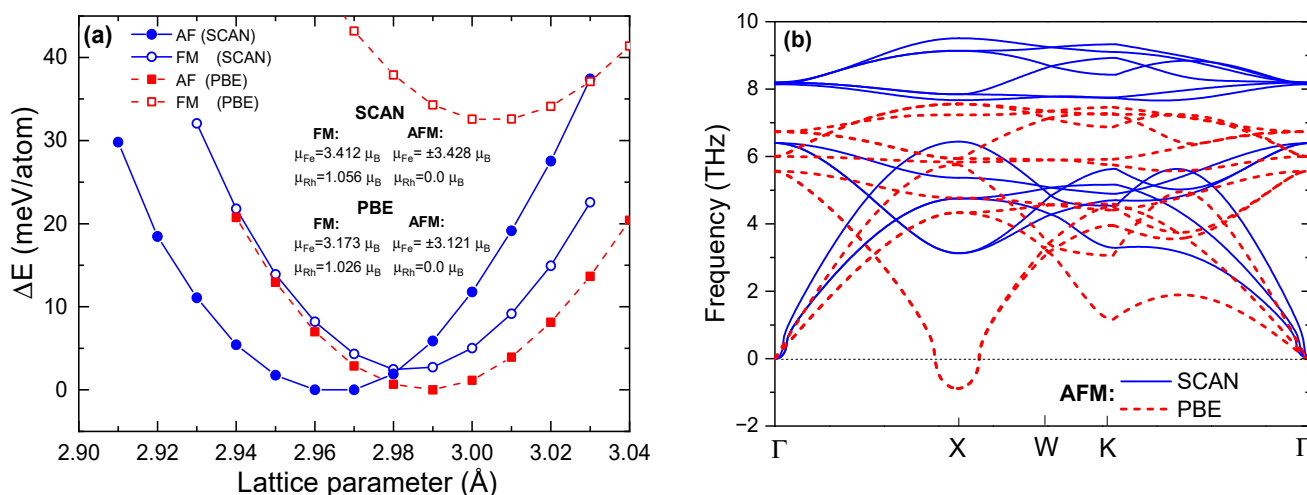


Figure 6. (a) Total energy difference versus the lattice parameter for the FM and AFM phases of FeRh alloy calculated within PBE and SCAN. The partial magnetic moments at corresponding optimized lattice parameters are also presented. (b) Phonon dispersion relations for AFM phase of FeRh alloy in the framework of SCAN and PBE calculations.

We now turn to a discussion of the calculated metamagnetic temperature between the AFM and FM phases as a function of applied pressure and compare these with the experimental data shown in Figure 7. To calculate the Gibbs energy for both FM and AFM phases, we consider only a lattice contribution through the quasi-harmonic Debye model [42,43], which allows us to calculate thermodynamic properties as a function of temperature and pressure from the DFT energy-volume $E(V)$ points and Debye temperatures taken from the phonon spectra calculations. It should be noted that the free-energy curves for FM and AFM phases calculated within the PBE $E(V)$ data do not intersect due to a large energy difference between the two phases that is in agreement with earlier theoretical works [54,56]. However, the consideration of SCAN $E(V)$ curves in combination with Θ_D as input in the Gibbs energy calculations predict well the transition temperature $T_m \sim 310$ K under ambient pressure, which is in good agreement with the experiment. This is mainly due to the smallest difference in the total energies of FM and AFM phases. However, an application of hydrostatic pressure up to 12 kbar leads to a sufficient increase in T_m up to 550 K, which contradicts the experimental data. The theoretical rate of change in T_m with pressure is $dT_m/dP \sim 20$ K/kbar, while the experiment gives ~ 3.4 K/kbar. It should be noted a similar effect of pressure has been observed in earlier theoretical calculations [17,18].

In order to resolve this contradiction, we considered the antisite defects in a high-temperature FM phase, which can occur in an ordered alloy when atoms of different types exchange their positions. For the investigation of point defects, we considered a periodically repeated supercell with 32, 64, 128, and 256 atoms, in which only one antisite pair (Fe–Rh) is embedded. Obviously, the larger the supercell, the lower the concentration of the antisite defect. As an example, the FM composition $(\text{Fe}_{15}\text{Rh}_1)\text{--}(\text{Rh}_{15}\text{Fe}_1)$ formed on a 32-atom defect supercell has the antisite defect fraction of 1/16. We denote this defect composition as FeRh@6.25%. In accordance with our calculations, there is no metamagnetic transition for this composition due to a large energy difference between both phases $\Delta E \approx 47$ meV/atom, whereas it takes place for compositions with a smaller defect concentration. As is evident from the P – T diagram, the transition temperature is only slightly affected by an applied pressure for FeRh@3.125% (the defect supercell with 64 atoms, $\Delta E \approx 23$ meV/atom). However, the further reduction in defect fraction in the FM phase by half reveals a good agreement between the theory and the experiment for FeRh@1.56% (the defect supercell with 128 atoms, $\Delta E \approx 16$ meV/atom). We would like to note that the subsequent change in the defect concentration results in an increase in the dT_m/dP slope, which becomes close to the case of pure AFM and FM phases, as exemplified by FeRh@0.78% (the defect supercell

with 256 atoms, $\Delta E \approx 3.7$ meV/atom). We are reminded that ΔE for compound with a pure FM and AFM phase is calculated to be 2.3 meV/atom, as shown in Figure 6a. Thus, we can conclude that the theoretical slope of dT_m/dP strongly depends on the defect concentration due to a change in ΔE and Θ_D between a pure AFM phase and a defect FM one.

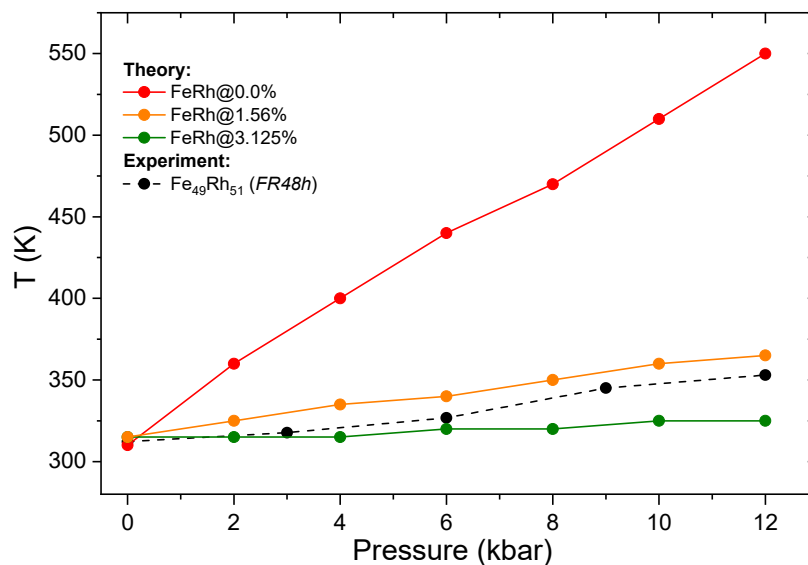


Figure 7. Theoretical and experimental T_m - P phase diagram for FeRh alloys. Theoretical $T_m(P)$ curves are calculated assuming pure AF and FM phases (label “FeRh@0.0%”) and the FM phase with one antisite pair embedded in the 64- and 128-atom supercell (labels “FeRh@3.125%” and “FeRh@1.56%”, respectively). The experimental curve $T_m(P)$ is obtained by averaging over the F_F , F_S , AF_S , and AF_F temperatures shown in Figure 5.

4. Conclusions

The effects of the high hydrostatic pressure up to 12 kbar and the high magnetic field up to 12 T on the stability of the MIPT in Fe₄₉Rh₅₁ alloy samples were studied. As expected, the strategy of the combination of the external fields leads to opposite contributions: the magnetic field expands the FM region and shifts the MIPT to the lower temperatures with the rate $dT_m/\mu_0 dH = -9.2$ K/T, and the hydrostatic pressure restores the stability of the AFM order and shifts the MIPT to the higher temperatures with the rate $dT_m/dP = 3.4$ K/kbar. The study of the multicaloric effect demonstrates that the hydrostatic pressure can be used for the tuning of the maximum of the magnetic entropy change, which has prospective applications for the upgrading of the magnetic cooling systems. The obtained experimental P - T diagram is explained by using the DFT calculations within the exchange correlation effects beyond the well-known GGA. The experimental dT_m/dP slope is reproduced theoretically when the antisite defects were considered in the computational supercell.

Author Contributions: Conceptualization, A.A.A.; Methodology, I.F.G., A.V.G. and V.I.V.; Software, V.V.S. and O.O.P.; Formal analysis, A.A.A. and V.I.V.; Investigation, A.P.K., A.A.A., V.D.Z., A.V.G. and V.V.S.; Writing—original draft, A.P.K. and A.A.A.; Supervision, V.D.B., A.M.A. and V.V.K.; Project administration, V.V.K., V.D.B. and A.M.A. All authors of the manuscript contributed equally to data acquisition and analysis, writing, editing and formatting. All authors have read and agreed to the published version of the manuscript.

Funding: The DSC and the electrical resistivity studies were carried out by A.P.K. and V.V.K. within the framework of the state task of Kotelnikov IRE RAS. V.V.S. acknowledges the financial support from the Priority-2030 Program of NUST “MISiS” (grant No. K2-2022-022) (the total energy calculations). O.O.P. and V.D.B. acknowledge the Ministry of Science and Higher Education of the Russian Federation within the Russian State Assignment, under Contract 075-01493-23-00 (the phonon calculations).

Data Availability Statement: The data presented in this study are available on request from the corresponding author.

Acknowledgments: The authors acknowledge Tino Gottschall from the High Magnetic Field Laboratory (HLD) at the Helmholtz-Zentrum Dresden-Rossendorf (HZDR), a member of the European Magnetic Field Laboratory (EMFL) for the help with the magnetization measurement in high magnetic fields.

Conflicts of Interest: The authors declare no conflict of interest.

References

1. Hofer, E.M.; Cucka, P. Magnetic properties of Rh-rich FeRh alloy. *J. Phys. Chem. Solids* **1966**, *27*, 1552–1555. [[CrossRef](#)]
2. Zakharov, A.I.; Kadomtseva, A.M.; Levitin, P.Z.; Ponyatovskii, E.G. Magnetic and magnetoelastic properties of a metamagnetic iron-rhodium alloy. *J. Exp. Theor. Phys.* **1964**, *19*, 1348–1353.
3. Belo, J.H.; Pires, A.L.; Araújo, J.P.; Pereira, A.M. Magnetocaloric materials: From micro- to nanoscale. *J. Mater. Res.* **2019**, *34*, 134–157. [[CrossRef](#)]
4. Zakharov, A. Crystal lattice parameter and structural distortions in Fe-Rh alloy at phase transitions. *Fiz. Met. I Metalloved.* **1967**, *24*, 84–90.
5. Lommel, J.M.; Kouvel, J.S. Effects of mechanical and thermal treatment on the structure and magnetic transitions in FeRh. *J. Appl. Phys.* **1967**, *38*, 1263–1264. [[CrossRef](#)]
6. Vinokurova, L.I.; Vlasov, A.V.; Pardavi-Horváth, M. Pressure effects on magnetic phase transitions in FeRh and FeRhIr alloys. *Phys. Status Solidi* **1976**, *78*, 353–357. [[CrossRef](#)]
7. Cherifi, R.O.; Ivanovskaya, V.; Phillips, L.C.; Zobelli, A.; Infante, I.C.; Jacquet, E.; Garcia, V.; Fusil, S.; Briddon, P.R.; Guiblin, N.; et al. Electric-field control of magnetic order above room temperature. *Nat. Mater.* **2014**, *13*, 345–351. [[CrossRef](#)]
8. Amirov, A.A.; Gottschall, T.; Chirkova, A.M.; Aliev, A.M.; Baranov, N.V.; Skokov, K.P.; Gutfleisch, O. Electric-field manipulation of the magnetocaloric effect in a Fe₄₉Rh₅₁/PZT composite. *J. Phys. D Appl. Phys.* **2021**, *54*, 505002. [[CrossRef](#)]
9. Qiao, K.; Wang, J.; Hu, F.; Li, J.; Zhang, C.; Liu, Y.; Yu, Z.; Gao, Y.; Su, J.; Shen, F.; et al. Regulation of phase transition and magnetocaloric effect by ferroelectric domains in FeRh/PMN-PT heterojunctions. *Acta Mater.* **2020**, *191*, 51–59. [[CrossRef](#)]
10. Sánchez-Valdés, C.F.; Gimaev, R.R.; López-Cruz, M.; Sánchez Llamazares, J.L.; Zverev, V.I.; Tishin, A.M.; Carvalho, A.M.G.; Aguiar, D.J.M.; Mudryk, Y.; Pecharsky, V.K. The effect of cooling rate on magnetothermal properties of Fe₄₉Rh₅₁. *J. Magn. Magn. Mater.* **2020**, *498*, 166130. [[CrossRef](#)]
11. Rodionov, V.; Amirov, A.; Annaorazov, M.; Lähderanta, E.; Granovsky, A.; Aliev, A.; Rodionova, V. Thermal hysteresis control in Fe₄₉Rh₅₁ alloy through annealing process. *Processes* **2021**, *9*, 772. [[CrossRef](#)]
12. Barua, R.; Jiménez-Villacorta, F.; Lewis, L.H. Towards tailoring the magnetocaloric response in FeRh-based ternary compounds. *J. Appl. Phys.* **2014**, *115*, 17A903. [[CrossRef](#)]
13. Tohki, A.; Aikoh, K.; Iwase, A.; Yoneda, K.; Kosugi, S.; Kume, K.; Batchuluun, T.; Ishigami, R.; Matsui, T. Effect of high temperature annealing on ion-irradiation induced magnetization in FeRh thin films. *J. Appl. Phys.* **2012**, *111*, 07A742. [[CrossRef](#)]
14. Kouvel, J.S.; Hartelius, C.C. Anomalous Magnetic Moments and Transformations in the Ordered Alloy FeRh. In Proceedings of the Seventh Conference on Magnetism and Magnetic Materials, Phoenix, AZ, USA, 13–16 November 1961; Springer: Boston, MA, USA, 1962; pp. 1343–1344. [[CrossRef](#)]
15. Richardson, M.J.; Melville, D.; Ricodeau, J.A. Specific heat measurements on an Fe Rh alloy. *Phys. Lett. A* **1973**, *46*, 153–154. [[CrossRef](#)]
16. Levitin, R.; Ponomarev, B. Magnetostriction of the Metamagnetic Iron-rhodium Alloy. *Sov. J. Exp. Theor. Phys.* **1966**, *23*, 984–985.
17. Mendive-Tapia, E.; Castán, T. Magnetocaloric and barocaloric responses in magnetovolumic systems. *Phys. Rev. B—Condens. Matter Mater. Phys.* **2015**, *91*, 224421. [[CrossRef](#)]
18. Gruner, M.E.; Entel, P. Simulation of the (p, T) phase diagram of the temperature-driven metamagnet α -FeRh. *Phase Transit.* **2005**, *78*, 209–217. [[CrossRef](#)]
19. Stern-Taulats, E.; Castán, T.; Planes, A.; Lewis, L.H.; Barua, R.; Pramanick, S.; Majumdar, S.; Mañosa, L. Giant multicaloric response of bulk Fe₄₉Rh₅₁. *Phys. Rev. B* **2017**, *95*, 104424. [[CrossRef](#)]
20. Stern-Taulats, E.; Planes, A.; Lloveras, P.; Barrio, M.; Tamarit, J.-L.; Pramanick, S.; Majumdar, S.; Frontera, C.; Mañosa, L. Barocaloric and magnetocaloric effects in Fe₄₉Rh₅₁. *Phys. Rev. B* **2014**, *89*, 214105. [[CrossRef](#)]
21. Nikitin, S.A.; Myalikgulyev, G.; Tishin, A.M.; Annaorazov, M.P.; Asatryan, K.A.; Tyurin, A.L. The magnetocaloric effect in Fe₄₉Rh₅₁ compound. *Phys. Lett. A* **1990**, *148*, 363–366. [[CrossRef](#)]
22. Nikitin, S.; Myalikgulyev, G.; Annaorazov, M.; Tyurin, A.L.; Myndyev, R.W.; Akopyan, S.A. Giant elastocaloric effect in FeRh alloy. *Phys. Lett. A* **1992**, *171*, 234–236. [[CrossRef](#)]
23. Gràcia-Condal, A.; Stern-Taulats, E.; Planes, A.; Mañosa, L. Caloric response of Fe₄₉Rh₅₁ subjected to uniaxial load and magnetic field. *Phys. Rev. Mater.* **2018**, *2*, 84413. [[CrossRef](#)]
24. Ponomarev, B.K. Investigation of the antiferro-ferromagnetism transition in an FeRh alloy in a pulsed magnetic field up to 300 kOe. *Sov. Phys. JETP* **1973**, *36*, 105–107.

25. Annaorazov, M.P.; Asatryan, K.A.; Myalikgulyev, G.; Nikitin, S.A.; Tishin, A.M.; Tyurin, A.L. Alloys of the FeRh system as a new class of working material for magnetic refrigerators. *Cryogenics* **1992**, *32*, 867–872. [[CrossRef](#)]
26. Aliev, A.M.; Batdalov, A.B.; Khanov, L.N.; Kamantsev, A.P.; Koledov, V.V.; Mashirov, A.V.; Shavrov, V.G.; Grechishkin, R.M.; Kaul, A.R.; Sampath, V. Reversible magnetocaloric effect in materials with first order phase transitions in cyclic magnetic fields: Fe₄₈Rh₅₂ and Sm_{0.6}Sr_{0.4}MnO₃. *Appl. Phys. Lett.* **2016**, *109*, 202407. [[CrossRef](#)]
27. Kamantsev, A.P.; Amirov, A.A.; Koshkid'ko, Y.S.; Mejía, C.S.; Mashirov, A.V.; Aliev, A.M.; Koledov, V.V.; Shavrov, V.G. Magnetocaloric Effect in Alloy Fe₄₉Rh₅₁ in Pulsed Magnetic Fields up to 50 T. *Phys. Solid State* **2020**, *62*, 160–163. [[CrossRef](#)]
28. Stern-Taulats, E.; Gràcia-Condal, A.; Planes, A.; Lloveras, P.; Barrio, M.; Tamarit, J.L.; Pramanick, S.; Majumdar, S.; Mañosa, L. Reversible adiabatic temperature changes at the magnetocaloric and barocaloric effects in Fe₄₉Rh₅₁. *Appl. Phys. Lett.* **2015**, *107*, 152409. [[CrossRef](#)]
29. Kamenev, V.I.; Kamenev, K.V.; Todris, B.M.; Zavadskii, E.A.; Varyukhin, V.N.; Baranov, N.V. Effect of pressure on magnetic phases of (Fe_{1-x}Ni_x)₄₉Rh₅₁. *High Press. Res.* **2003**, *23*, 195–199. [[CrossRef](#)]
30. Batdalov, A.B.; Aliev, A.M.; Khanov, L.N.; Kamantsev, A.P.; Mashirov, A.V.; Koledov, V.V.; Shavrov, V.G. Specific heat, electrical resistivity, and magnetocaloric study of phase transition in Fe₄₈Rh₅₂ alloy. *J. Appl. Phys.* **2020**, *128*, 013902. [[CrossRef](#)]
31. Amirov, A.A.; Tishin, A.M.; Pakhomov, O.V. Multicalorics—New materials for energy and straintronics (Review). *Phys. Solid State* **2022**, *64*, 383. [[CrossRef](#)]
32. Stern-Taulats, E.; Castán, T.; Mañosa, L.; Planes, A.; Mathur, N.D.; Moya, X. Multicaloric materials and effects. *MRS Bull.* **2018**, *43*, 295–299. [[CrossRef](#)]
33. Gottschall, T.; Bykov, E.; Gràcia-Condal, A.; Beckmann, B.; Taubel, A.; Pfeuffer, L.; Gutfleisch, O.; Mañosa, L.; Planes, A.; Skourski, Y.; et al. Advanced characterization of multicaloric materials in pulsed magnetic fields. *J. Appl. Phys.* **2020**, *127*, 185107. [[CrossRef](#)]
34. Gottschall, T.; Gràcia-Condal, A.; Fries, M.; Taubel, A.; Pfeuffer, L.; Mañosa, L.; Planes, A.; Skokov, K.P.; Gutfleisch, O. A multicaloric cooling cycle that exploits thermal hysteresis. *Nat. Mater.* **2018**, *17*, 929–934. [[CrossRef](#)] [[PubMed](#)]
35. Amirov, A.A.; Starkov, A.S.; Starkov, I.A.; Kamantsev, A.P.; Rodionov, V.V. Electric field controlled magnetic phase transition in Fe₄₉Rh₅₁ based magnetoelectric composites. *Lett. Mater.* **2018**, *8*, 353–357. [[CrossRef](#)]
36. Val'kov, V.I.; Varyukhin, D.V.; Golovchan, A.V.; Gribov, I.F.; Sivachenko, A.P.; Kamenev, V.I.; Todris, B.M. Influence of pressure on the stability of the magnetically ordered states in alloys of the system Mn_{2-x}Fe_xAs_{0.5}P_{0.5}. *Low Temp. Phys.* **2008**, *34*, 734–745. [[CrossRef](#)]
37. Wien, T.U.; Hauptstrage, W. Ab Initio Molecular-Dynamics Simulation of the Liquid-Metal-Amorphous-Semiconductor Transition in Germanium. *Phys. Rev. B* **1994**, *49*, 14251–14269.
38. Kresse, G.; Furthmüller, J. Efficiency of ab-initio total energy calculations for metals and semiconductors using a plane-wave basis set. *Comput. Mater. Sci.* **1996**, *6*, 15–50. [[CrossRef](#)]
39. Perdew, J.P.; Burke, K.; Ernzerhof, M. Generalized gradient approximation made simple. *Phys. Rev. Lett.* **1996**, *77*, 3865–3868. [[CrossRef](#)]
40. Sun, J.; Ruzsinszky, A.; Perdew, J. Strongly Constrained and Appropriately Normed Semilocal Density Functional. *Phys. Rev. Lett.* **2015**, *115*, 036402. [[CrossRef](#)]
41. Togo, A.; Oba, F.; Tanaka, I. First-principles calculations of the ferroelastic transition between rutile-type and CaCl₂-type SiO₂ at high pressures. *Phys. Rev. B—Condens. Matter Mater. Phys.* **2008**, *78*, 134106. [[CrossRef](#)]
42. Otero-De-La-Roza, A.; Luaña, V. Gibbs2: A new version of the quasi-harmonic model code. I. Robust treatment of the static data. *Comput. Phys. Commun.* **2011**, *182*, 1708–1720. [[CrossRef](#)]
43. Otero-De-La-Roza, A.; Abbasi-Pérez, D.; Luaña, V. Gibbs2: A new version of the quasiharmonic model code. II. Models for solid-state thermodynamics, features and implementation. *Comput. Phys. Commun.* **2011**, *182*, 2232–2248. [[CrossRef](#)]
44. Kamantsev, A.P.; Koledov, V.V.; Mashirov, A.V.; Dilmieva, E.T.; Shavrov, V.G.; Cwik, J.; Tereshina, I.S.; Lyange, M.V.; Khovaylo, V.V.; Porcari, G.; et al. Properties of metamagnetic alloy Fe₄₈Rh₅₂ in high magnetic fields. *Bull. Russ. Acad. Sci. Phys.* **2015**, *79*, 1086–1088. [[CrossRef](#)]
45. Tishin, A.M.; Spichkin, Y.I. *The Magnetocaloric Effect and Its Applications*; Taylor & Francis: Abingdon, UK, 2003; ISBN 0-7503-0922-9.
46. Wang, Y.; Wang, H.; Tan, W.; Huo, D. Magnetization reversal, critical behavior, and magnetocaloric effect in NdMnO₃: The role of magnetic ordering of Nd and Mn moments. *J. Appl. Phys.* **2022**, *132*, 183907. [[CrossRef](#)]
47. Zhao, B.; Hu, X.; Dong, F.; Wang, Y.; Wang, H.; Tan, W.; Huo, D. The Magnetic Properties and Magnetocaloric Effect of Pr_{0.7}Sr_{0.3}MnO₃ Thin Film Grown on SrTiO₃ Substrate. *Materials* **2023**, *16*, 75. [[CrossRef](#)] [[PubMed](#)]
48. Amirov, A.A.; Cugini, F.; Kamantsev, A.P.; Gottschall, T.; Solzi, M.; Aliev, A.M.; Spichkin, Y.I.; Koledov, V.V.; Shavrov, V.G. Direct measurements of the magnetocaloric effect of Fe₄₉Rh₅₁ using the mirage effect. *J. Appl. Phys.* **2020**, *127*, 233905. [[CrossRef](#)]
49. Isaacs, E.B.; Wolverton, C. Performance of the strongly constrained and appropriately normed density functional for solid-state materials. *Phys. Rev. Mater.* **2018**, *2*, 63801. [[CrossRef](#)]
50. Ekholm, M.; Gambino, D.; Jönsson, H.J.M.; Tasnádi, F.; Alling, B.; Abrikosov, I.A. Assessing the SCAN functional for itinerant electron ferromagnets. *Phys. Rev. B* **2018**, *98*, 94413. [[CrossRef](#)]
51. Buchelnikov, V.D.; Sokolovskiy, V.V.; Miroshkina, O.N.; Zagrebina, M.A.; Nokelainen, J.; Pulkkinen, A.; Barbiellini, B.; Lähderanta, E. Correlation effects on ground-state properties of ternary Heusler alloys: First-principles study. *Phys. Rev. B* **2019**, *99*, 14426. [[CrossRef](#)]

52. Baigutlin, D.R.; Sokolovskiy, V.V.; Miroshkina, O.N.; Zagrebin, M.A.; Nokelainen, J.; Pulkkinen, A.; Barbiellini, B.; Pussi, K.; Lähderanta, E.; Buchelnikov, V.D.; et al. Electronic structure beyond the generalized gradient approximation for Ni₂MnGa. *Phys. Rev. B* **2020**, *102*, 45127. [[CrossRef](#)]
53. Buchelnikov, V.D.; Sokolovskiy, V.V.; Miroshkina, O.N.; Baigutlin, D.R.; Zagrebin, M.A.; Barbiellini, B.; Lähderanta, E. Prediction of a Heusler alloy with switchable metal-to-half-metal behavior. *Phys. Rev. B* **2021**, *103*, 54414. [[CrossRef](#)]
54. Wolloch, M.; Gruner, M.E.; Keune, W.; Mohn, P.; Redinger, J.; Hofer, F.; Suess, D.; Podloucky, R.; Landers, J.; Salamon, S.; et al. Impact of lattice dynamics on the phase stability of metamagnetic FeRh: Bulk and thin films. *Phys. Rev. B* **2016**, *94*, 174435. [[CrossRef](#)]
55. Belov, M.P.; Syzdykova, A.B.; Abrikosov, I.A. Temperature-dependent lattice dynamics of antiferromagnetic and ferromagnetic phases of FeRh. *Phys. Rev. B* **2020**, *101*, 134303. [[CrossRef](#)]
56. Vieira, R.M.; Eriksson, O.; Bergman, A.; Herper, H.C. High-throughput compatible approach for entropy estimation in magnetocaloric materials: FeRh as a test case. *J. Alloys Compd.* **2021**, *857*, 157811. [[CrossRef](#)]

Disclaimer/Publisher's Note: The statements, opinions and data contained in all publications are solely those of the individual author(s) and contributor(s) and not of MDPI and/or the editor(s). MDPI and/or the editor(s) disclaim responsibility for any injury to people or property resulting from any ideas, methods, instructions or products referred to in the content.